Quantitative study of kinetic ballooning mode theory in simple geometry

K. Aleynikova, A. Zocco

Max-Planck-Institut für Plasmaphysik, D-17491, Greifswald, Germany

Abstract

The theory of kinetic ballooning modes (KBMs) in a magnetically confined toroidal plasma is studied analytically and numerically by means of gyrokinetic simulations. A physics-based ordering for β (the ratio of kinetic to magnetic plasma pressure) with small asymptotic parameters is found. This allows us to derive several simplified limits of previously known theories. We introduce a variational approach which provides explicit dispersion relations in terms of integrals of quadratic forms constructed from numerical eigenfunctions. It is found that, for large pressure gradients, the growth rate and frequencies computed by gyrokinetic codes show excellent agreement with those evaluated by using a diamagnetic modification of ideal MHD if geometric drifts are kept consistent with the equilibrium pressure gradient. For moderate pressure gradients, a new finite-β formulation of KBM theory is proposed. Also in this case, good agreement between numerical simulations and analytical theory is found.

I. INTRODUCTION

In a toroidal magnetic fusion device, the curvature of the confining magnetic field and the plasma pressure gradient cause a destabilization of hydromagnetic modes with long wavelengths along and short wavelengths across the magnetic field. The nature of the drive of the instability, which is inextricably related to magnetic field and pressure gradients, makes such instabilities rather pervasive.

The high-mode-number toroidal instabilities were first successfully studied within the ideal magnetohydrodynamic (MHD) model using the ballooning transform [1]. Accounting for kinetic effects lead to the development of a framework for the study of Kinetic Ballooning Modes (KBM) [2, 3]. The equations that describe kinetic ballooning modes were put forward in the seminal works of Antonsen and Lane [2], and of Tang, Connor and Hastie [3]. However, the complex structure of the general equations presented by these authors prevents a straightforward analytical prediction for the KBM.

Kinetic ballooning modes are routinely observed in finite-β gyrokinetic numerical simulations under the same conditions that would produce an electrostatic ion-temperature-gradient (ITG) driven instability [4–6].

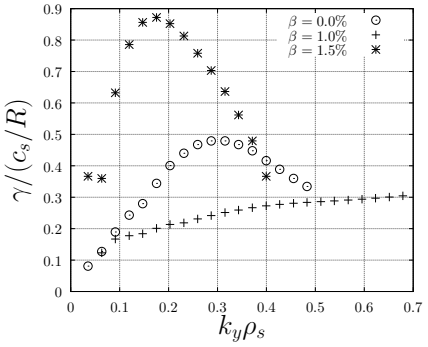

Figure 1. A typical transition of the spectrum of microinstabilities in a local flux tube simulation. From electrostatic ITG ($\beta = 0\%$) to KBM ($\beta = 1.5\%$). Here γ is the growth rate, $k_y\rho_s$ the mode wavelength, with ρ_s the sound ion Larmor radius.

In this context, the parameter $\beta = 8\pi p/B^2$, the ratio of plasma to magnetic pressure, is a measure of the importance of electromagnetic effects. The typical β-dependence of

these instabilities is illustrated in Fig. 1, which shows the growth rate of the most unstable microinstabilities evaluated with local flux-tube simulations. The electrostatic ITG mode ($\beta = 0\%$) is partly stabilized by a finite $\beta \sim 1\%$. For larger β, a long-wavelength mode gets destabilized: the KBM.

To date, it is not clear under which circumstances gyrokinetic simulations of the finite β temperature-gradient-driven microinstability produce results compatible with the theory of ideal ballooning modes. The purpose of this work is to shed light on this matter.

We extend a recent electromagnetic analysis of ITG modes [7] and derive an optimal ordering for all relevant expansion parameters that allows us to greatly simplify the original KBM equation of Ref [3]. It is shown that, at long-wavelengths, a finite-β theory of KBMs can be adequately described by a simple diamagnetic modification of the ideal MHD equation as long as local magnetic drifts are kept consistent to the equilibrium constraint $\mathbf{j}\times\mathbf{B} = \nabla\mathbf{p}$.

This analytical result is then tested numerically with the gyrokinetic codes GS2 [8, 9] and GENE [10, 11] by using a simple $\hat{s} - \alpha$ equilibrium model [1]. We assess the quantitative effect of the equilibrium constraint on the instability and predict the KBM growth rate for both large and moderate temperature gradients.

For large temperature gradients, the gyrokinetic codes show excellent quantitative agreement with a diamagnetic modification of ideal MHD. In this case, instability occurs only for $Re(\omega) \equiv \omega_r = \omega_{pi}/2$, where ω the complex mode frequency, ω_r is its real part and ω_{pi} the ion diamagnetic frequency associated with the ion pressure gradient. The instability is most unstable at long wavelength. For moderate temperature gradients, we observe that the mode frequency tends to a value $\omega_r > \omega_{pi}/2$. The maximum growth rate occurs at small but finite wavelength. A higher-order theory that generalizes the intermediate-frequency regime of Ref. [3] to finite β is also introduced. The moderate-gradient regime is quantitatively described by this theory.

This work is structured in the following way: in Section II, we derive the natural ordering of β and $b = k_\perp^2\rho_i^2/2$, with ρ_i the ion Larmor radius that allows us simplify the general KBM theory of Ref. [3]. In Section III we introduce a variational approach which allows us to verify numerically the analytical results of the Section II. The conclusions are summarized in Section IV. The appendices include information about velocity-space integrals (Appendix A), GS2 and GENE gyrokinetic codes benchmark (Appendix B) and the influence of magnetic shear on KBM stability (Appendix C).

II. HIGH$-\beta$ ORDERING FOR KBMs

The basic theory of kinetic ballooning modes was developed in Ref. [3]. Here, the authors solve the gyrokinetic equation by expanding in $\varepsilon = v_{thi}^2/\omega^2 l_c^2 \ll 1$, where v_{thi} is the ion thermal speed, l_c the connection length and $\omega \ll v_{the}/l_c$ is the mode frequency, with v_{the} the electron thermal speed. The general KBM equation retains magnetic drift resonances, gyro-averaging and magnetic compressibility effects. The result is a second order differential equation for the electrostatic potential ϕ, that reads:

$$\frac{1}{\beta_i B}\frac{2v_{ths}^2/l_c^2}{\omega^2}\frac{\partial}{\partial z}bB\frac{\partial\phi}{\partial z} = K\phi, \tag{1}$$

with

$$\begin{aligned} K = &\left\{\left[Q - \left(1 - \frac{\omega_{*i}}{\omega}\right)\right]\left[\alpha_{0,e}\left(1 + \frac{\beta_i}{2}R\right) - \alpha_{1,e}\tau Q'\frac{\beta_i}{2}\right]\right. \\ &\left. - \frac{\beta_i}{2}\left(Q' + \alpha_{1,e}\right)\left[\alpha_{0,e}Q' + \alpha_{1,e}\left(1 + \tau - \tau Q\right)\right]\right\} \times \left\{\left(1 + \tau - \tau Q\right)\left(1 + \frac{\beta_i}{2}R\right) + \tau Q'^2\frac{\beta_i}{2}\right\}^{-1} \\ &- \alpha_{1,e}\frac{\omega_\kappa + \omega_B}{\omega}, \end{aligned} \tag{2}$$

where the normalization length l_c and the coordinate z along the field are defined so that $l_c\nabla_\parallel = \partial_z$, $\alpha_{n,j} = 1 - (\omega_{*i}/\omega)(1 + n\eta_j)$, $\tau = T_i/T_e$, $\eta_i = L_{n_i}/L_{T_i}$, $\omega_{*i} = \frac{1}{2}k_y\rho_{i,e}v_{th}/L_n$. Furthermore:

$$Q = \int d^3v \frac{F_0}{n_0} J_0^2\left(\frac{\omega - \omega_*^T}{\omega - \omega_d}\right), \tag{3}$$

$$Q' = \int d^3v \frac{F_0}{n_0}\frac{d}{db} J_0^2\left(\frac{\omega - \omega_*^T}{\omega - \omega_d}\right), \tag{4}$$

$$R = \frac{2}{b}\int d^3v \frac{F_0}{n_0} v_\perp^4 J_1^2\left(\frac{\omega - \omega_*^T}{\omega - \omega_d}\right), \tag{5}$$

with

$$\begin{aligned} \omega_d &= 2\left(\omega_B\frac{v_\perp^2}{2} + \omega_\kappa v_\parallel^2\right), \\ \omega_B &= \frac{k_y\rho_i}{2}\frac{v_{thi}}{R}\Big[\cos z + (\hat{s}z - \alpha\sin z)\sin z\Big], \\ \omega_\kappa &= \omega_B + \frac{k_y\rho_i}{2}\frac{v_{thi}}{R}\frac{\alpha}{2q^2} \\ &\equiv \frac{k_y\rho_i}{2}\frac{v_{thi}}{R}\Big[\cos z + (\hat{s}z - \alpha\sin z)\sin z\Big] + \frac{\beta_i}{2}\Big[\omega_{*i}\left(1 + \eta_i\right) - \omega_{*e}\left(1 + \eta_e\right)\Big] \end{aligned} \tag{6}$$

where F_0 is the Maxwellian distribution function with density n_0, q is the safety factor and $\alpha = -Rq^2\beta'$ is the normalized pressure gradient parameter, where $\beta' = \beta_i\big[\omega_{*i}\,(1+\eta_i) - \omega_{*e}\,(1+\eta_e)\,\big]$. We consider a circular $\hat{s}-\alpha$ equilibrium model. Eq. (1) has a complex structure, but it can be significantly simplified under certain conditions.

In the long-wavelength $b \ll 1$, non-resonant limit $b \sim \omega_d/\omega$, $Q \to 1 - \frac{\omega_{*i}}{\omega} + O(\varepsilon)$, as seen from Eq. (15) in Appendix A. Therefore, the first term of the numerator of Eq. (2) in the first pair of the curly brackets cancels to zeroth order, restricting the second term in the first curly brackets (which is order β, since $\alpha_{i,j} \sim 1$) to order ε i.e. $\beta \sim \varepsilon$. The last term of the right-hand side of Eq. (2) (in order to compete with the first term) is of the same order as the first just discussed and is retained when $\omega_d/\omega \sim \varepsilon$. The resulting ordering is $\beta \sim b \sim \omega_d/\omega \sim \varepsilon$, which is consistent with the fact that with increasing temperature gradient the KBM tends to have maximum growth rate at long wavelengths (i.e. $b \sim \varepsilon$). We refer to $\beta \sim \varepsilon$ as the "high-β ordering" as opposed to the low-β ordering $\beta \sim \varepsilon^2$ of Ref. [7].

Thus, expanding K to first order in ε, Eq.(1) takes the form:

$$\frac{1}{\beta_i}\frac{v_{thi}^2}{\omega^2 l_c^2}\frac{\partial}{\partial z}bB\frac{\partial\phi}{\partial z} = -\frac{\omega_B+\omega_\kappa}{\omega^2}\omega_p\phi - b\alpha_{1,i}\phi - \frac{\beta_i}{2}\frac{{\omega_p}^2}{\omega^2}\phi, \tag{7}$$

where $\omega_p = \omega_{*i}\,(1+\eta_i) - \omega_{*e}\,(1+\eta_e) \equiv \omega_{pi} + \omega_{pe}$.

Note here that our high-β ordering does not permit us to use the common approximation $\omega_\kappa \approx \omega_B$. Equation (6) can be rewritten as $(\beta_i/2)\omega_p^2/\omega^2 = (\omega_\kappa - \omega_B)\omega_p/\omega^2$ [3]. Equation (7) is thus the familiar ideal-MHD equation with a diamagnetic correction [12]:

$$\underbrace{\frac{1}{\beta_i}\frac{v_{thi}^2}{\omega^2 l_c^2}\frac{\partial}{\partial z}bB\frac{\partial\phi}{\partial z}}_{field\ line\ bending} = \underbrace{-\frac{2\omega_\kappa\omega_p}{\omega^2}\phi}_{curvature} - \underbrace{b\big[1-\frac{\omega_{*i}}{\omega}(1+\eta_i)\big]\phi}_{diamagnetic}. \tag{8}$$

Equation (8) is much simpler than Eq. (1), and yet takes into account FLR effects (through the last term) and magnetic compressibility at high $\beta \sim \varepsilon$. This is an unexpected result, since electromagnetic corrections, in particular magnetic compressibility, have a zeroth-order effect on the electromagnetic ITG for $\beta \sim \varepsilon^2$ [see Eq.(22) of Ref. [7]], and yet Eq. (8) (derived for $\beta \sim \varepsilon$) coincides with Eq.(20) of Ref. [7] for the electromagnetic ITG when $\eta_i \gg 1$. Section III demonstrates that this equation is an adequate approximation of the high-temperature-gradient regime of KBM.

For moderate temperature-gradients, as we shall see, the frequency of the mode increases, making the field-line-banding term on the LHS of Eq. (1) smaller, and compelling us to

consider higher-order terms on the RHS of Eq. (1). The extent to which such small terms ought to be retained is dictated by the action of the equilibrium pressure gradient. We can see how we must include terms that are second order in the original ordering $b \sim \omega_d/\omega \sim \varepsilon$. Indeed, the driving term is $\omega_\kappa \omega_p/\omega^2 \sim k_y^2 \rho_i^2 v_{thi}^2/(R L_p \omega^2)$, which tends to be not a function of $k_y \rho_i$ for $\omega \propto k_y \rho_i$ and starts, for decreasing R/L_T, competing with $\omega_\kappa^2/\omega^2 \sim k_y^2 \rho_i^2 v_{thi}^2/(R^2 \omega^2)$ which is formally $O(\varepsilon^2)$. Thus, for moderate pressure gradients, a decreasing R/L_p tends to render the next order correction of the original ordering non negligible.

With all second-order (in ε) terms, Eq. (1) takes the form:

$$\frac{1}{\beta_i}\frac{v_{thi}^2}{\omega^2 l_c^2}\frac{\partial}{\partial z} bB \frac{\partial \phi}{\partial z} = -\frac{2\omega_\kappa \omega_p}{\omega^2}\phi - b\alpha_{1,i}\phi + \underbrace{\frac{(\omega_\kappa+\omega_B)^2}{\omega^2}\tau\frac{\alpha_{1,i}^2}{\alpha_{0,e}}\phi + 2\frac{\frac{3}{2}\omega_\kappa^2+\omega_B\omega_\kappa+\omega_B^2}{\omega^2}\alpha_{2,i}\phi}_{\text{(A)}:\ \frac{\omega_d^2}{\omega^2}\sim\varepsilon^2} -$$

$$\underbrace{-\frac{2(\omega_\kappa+\omega_B)}{\omega}b\tau\frac{\alpha_{1,i}^2}{\alpha_{0,e}}\phi + b^2(\tau\frac{\alpha_{1,i}^2}{\alpha_{0,e}}+\frac{\alpha_{2,i}}{8})\phi - b\alpha_{2,i}\frac{\omega_\kappa+2\omega_B}{\omega}\phi}_{\text{(B)}:\ \frac{\omega_d}{\omega}b\sim b^2\sim\varepsilon^2} +$$

$$\underbrace{+\beta_i\alpha_{2,i}\omega_p\frac{2\omega_\kappa+\omega_B}{\omega^2}\phi + \frac{\beta_i^2}{4}\frac{\omega_p^2}{\omega^2}(\tau\frac{\alpha_{1,i}^2}{\alpha_{0,e}}+\frac{3}{2}\alpha_{3,i})\phi + (\frac{\omega_\kappa+\omega_B}{\omega}}_{\text{(C)}:\ \frac{\omega_d}{\omega}\beta\sim\beta^2\sim\varepsilon^2}\underbrace{-b)\tau\beta_i\frac{\alpha_{1,i}^2}{\alpha_{0,e}}\frac{\omega_p}{\omega}\phi - \frac{3}{2}b\beta_i\alpha_{2,i}\frac{\omega_p}{\omega}\phi}_{\text{(D)}:\ b\beta\sim\varepsilon^2}, \tag{9}$$

where the origin of each contribution is given. For more details see Appendix A. This equation is found to approximate KBM modes in a broad range of parameters, as discussed in Section III. While Eq. (9) might look cumbersome, it is sufficient to describe KBMs for realistic pressure gradients.

Let us be more specific about possible subsidiary expansions . In particular, the balance of the $O(\varepsilon)$ terms of Eq. (9) gives:

$$\omega \sim \sqrt{\frac{\omega_\kappa \omega_p}{b}},$$

suggesting the existence of three small expansion parameters:

$$\beta \ll 1, \quad b \ll 1, \quad \frac{\omega_\kappa}{\omega_p} \sim \delta = \frac{L_p}{R} \ll 1.$$

The comparison of the first term on the right-hand side of Eq. (9) and the first term from group A gives:

$$\frac{(\omega_\kappa+\omega_B)^2}{\omega^2}\Big/\frac{\omega_\kappa\omega_p}{\omega^2} \sim \frac{\omega_\kappa}{\omega_p} \sim \delta,$$

which only scales with L_p/R. The same procedure applied to the other groups of Eq. (9) gives for group B:

$$\frac{\omega_\kappa+\omega_B}{\omega}b\Big/b\sim\frac{\omega_\kappa}{\omega}\sim\sqrt{\frac{b\omega_\kappa}{\omega_p}}\sim\sqrt{b\delta};$$

for group C:

$$\beta\omega_p\frac{2\omega_\kappa+\omega_B}{\omega^2}\Big/\frac{\omega_\kappa\omega_p}{\omega^2}\sim\beta;$$

for group D:

$$b\beta\frac{\omega_p}{\omega}\Big/b\sim\beta\frac{\omega_p}{\omega}\sim\beta\sqrt{\frac{b\omega_p}{\omega_\kappa}}\sim\beta\sqrt{\frac{b}{\delta}}.$$

For small b, the terms of group B and D are negligible. Those of group C are relevant only for very large gradients ($L_p/R\sim\beta$) therefore can be neglected in a moderate gradient regime. For finite-β, terms of group D will set an upper bound for negligible second order terms, because of their β dependence.

Therefore, as pressure gradients decrease, δ increases making terms of group A (which only scale with δ) increasingly important. Formally, this occurs for:

$$\beta^{2/3}b^{1/3}\ll\frac{L_p}{R}\ll\frac{1}{\beta}.$$

In this limit Eq. (9) simplifies significantly:

$$\frac{1}{\beta_i}\frac{v_{thi}^2}{\omega^2l_c^2}\frac{\partial}{\partial z}bB\frac{\partial\phi}{\partial z}=-\frac{2\omega_\kappa\omega_p}{\omega^2}\phi-b\alpha_{1,i}\phi+\frac{(\omega_\kappa+\omega_B)^2}{\omega^2}\tau\frac{\alpha_{1,i}^2}{\alpha_{0,e}}\phi+2\frac{\frac{3}{2}\omega_\kappa^2+\omega_B\omega_\kappa+\omega_B^2}{\omega^2}\alpha_{2,i}\phi. \quad (10)$$

This equation indeed represents the long wavelength limit of KBMs as shown in Section III.

In Ref.[3] an ideal-MHD limit of the KBM Eq. (1) was suggested to take the form [Eq. (3.40)]:

$$\frac{1}{\beta_i}\frac{v_{thi}^2}{\omega^2l_c^2}\frac{\partial}{\partial z}bB\frac{\partial\phi}{\partial z}=-\frac{2\omega_\kappa\omega_p}{\omega^2}\phi-b\alpha_{1,i}\phi+\frac{\omega_\kappa^2}{\omega^2}[7\alpha_{2,i}+4\tau\frac{\alpha_{1,i}^2}{\alpha_{0,e}}]\phi, \quad (11)$$

where a typo has been corrected. Although Eq. (11) resembles Eq. (8) and Eq. (10), it appears to be more limited than the latter two due to the aforementioned lack of ordering in β. Equation (11) was derived from Eq. (1) in the limit where b and ω_d/ω are small parameters and $\beta\ll1$, but the authors do not specify how small β should be. We notice that Eq. (11) is indeed recovered from Eq. (10) if we set $\omega_\kappa=\omega_B$. Here, we can only say that, for this to be true, β and β' must be both small enough to set $\omega_\kappa=\omega_B$. This can perhaps be achieved with a subsidiary ultra-low β expansion which, however, must be kept consistent to the original high-β ordering ($\beta\sim\varepsilon$).

In the next sections the validity of Eqs. (8)-(10) in different regimes will be checked against numerical simulations with the GENE and GS2 codes.

III. NUMERICAL VERIFICATION

When the coefficients of Eqs. (8)-(10) are constant, a Fourier analysis is possible. This is done for Eq. (8) in Appendix D. However, pursuing the goal to examine the characteristics of KBMs in toroidal geometry, we introduce a variational approach.

Equations (8)-(10) are multiplied by the complex conjugate ϕ^* and integrated by parts resulting in the following relation for ω:

$$\omega(\omega-\omega_{p_i})\int_{-\infty}^{\infty}\frac{b|\phi|^2}{B}dz=-2\omega_p\int_{-\infty}^{\infty}\frac{\omega_\kappa|\phi|^2}{B}dz+\frac{1}{\beta_i}\frac{v_{thi}^2}{l_c^2}\int_{-\infty}^{\infty}b\Big|\frac{\partial\phi}{\partial z}\Big|^2dz, \tag{12}$$

where we are showing the procedure for Eq.(8) for illustrative purposes. For each k_y, we substitute the eigenfunctions ϕ obtained with the GENE code, perform the integration and solve for the complex ω. The result is then compared to the original eigenvalue given by GENE.

3.1. SIMULATION DETAILS

We consider hydrogen plasma and Cyclone Base Case (CBC, Ref.[13]) parameters in the collisionless regime, in the simple $\hat{s}-\alpha$ geometry, with electromagnetic effects and consistent pressure gradients (see Appendix B for benchmark details and GS2-GENE comparison), therefore: $T_i/T_e=1$, $m_i/m_e=1836$, $R/L_{ni,e}=2.22$, $R/L_{Ti,e}=6.89$, $r/a=0.5$, $R/a=2.7775$, $r/R=0.18$, $q=1.4$, $\hat{s}=0.786$. Here, $T_{i,e}$ are the ion and electron temperature, R is the major radius, r is the minor radius, $L_{Ti,e}$ and L_n are the characteristic gradient lengths for temperature and density, a is a GS2 equilibrium reference normalization length (we use the value $a=1.08$ m) and $\hat{s}$ is the magnetic shear. In the present work β is defined as:

$$\beta_{GS2/GENE}=\beta_{i,e}=\frac{\beta}{2}=\frac{8\pi n_{i0}T_{ref}}{B_{ref}^2},$$

where T_{ref} is a reference temperature, B_{ref} a reference magnetic field and n_{i_0} is the equilibrium ion density. Note that $\beta_{GS2/GENE}=\beta_{total}/2$.

The curvature and ∇B drift frequencies in code units are:

$$\omega_B = \frac{k_y \rho_{ref}}{2} \frac{v_{ref}}{L_{ref}} \left\{ \cos z + (\hat{s} z - \alpha \sin z) \sin z \right\}, \tag{13}$$

$$\omega_\kappa = \frac{k_y \rho_{ref}}{2} \frac{v_{ref}}{L_{ref}} \left\{ \cos z + (\hat{s} z - \alpha \sin z) \sin z + \frac{\beta}{2} \Big[\frac{R}{L_{Ti}} + \tau \frac{R}{L_{Te}} + (1+\tau) \frac{R}{L_n} \Big] \Big(1 + \frac{r}{R} \cos z \Big)^2 \right\}. \tag{14}$$

The extra part of curvature drift connected with the pressure gradient was implemented in the GS2 code and verified using GENE results (see Appendix B, Fig.6). All data (unless stated otherwise) were obtained considering this additional part of curvature drift. Note that $b = k_y^2 \rho_i^2 / 2[1 + (\hat{s} z - \alpha \sin z)^2]$, $B = B_0 (1 + r/R \cos z)^{-1}$, which is also used in our variational analysis.

3.2. RESULTS

Equation (12) implies that a necessary condition for instability is $Re(\omega) = \omega_{p_i}/2$. This is indeed observed for large temperature gradients. Thus we consider two distinct regimes: *large temperature gradients*, where, we argue, Eq. (8) is appropriate, and *moderate temperature gradients*, where corrections given in Eq. (9) will be required.

3.2.1. LARGE TEMPERATURE GRADIENTS

The KBMs obtained from GENE (solid curves) and from the variational approach of Eq. (12) are shown in Fig.2. Here $\beta = 1.5\%, q = 1.4$, $R/L_{ni,e} = 2.22$ and $R/L_{Ti,e} = 35, 40, 45$. Note that ω_r is the real part of the complex frequency in Eqs. (8)-(10).

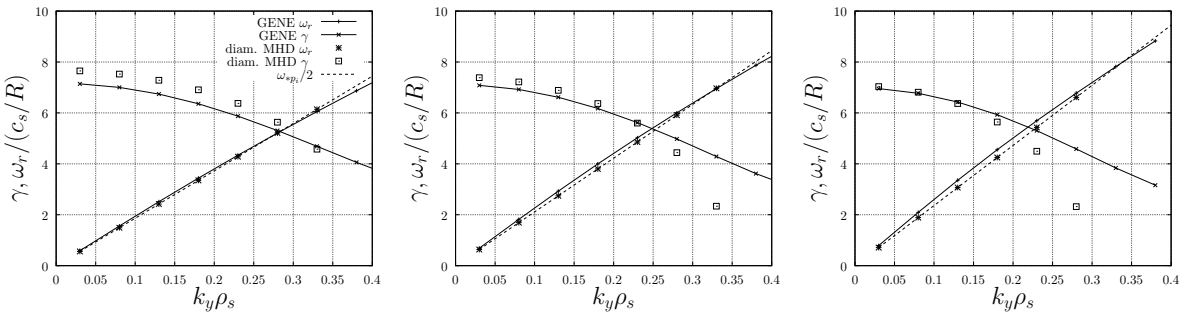

Figure 2. Spectra for $R/L_{Ti,e} = 35, 40, 45$ from left to right respectively. On the plot GENE simulations γ: solid curve ($\times$) and ω_r: solid curve ($+$) against results obtained solving Eq. (8) (γ: squares and ω_r: stars) are presented. The dashed line represents the $\omega_{*pi}/2$ frequency.

We stress the importance of the real frequency in the identification of different KBM regimes. This aspect has been neglected in many numerical studies in the literature. The frequency of the mode is indeed $\omega_r \approx \omega_{pi}/2$. The maximum growth rate is at $k_y = 0$, where $\omega_r \approx 0$. The agreement of the GENE results and our model is excellent and improves with increasing temperature gradient.

This comparison shows that the suggested simplified model of ideal MHD with diamagnetic correction [i.e. Eq. (8)] appears to reasonably approximate the quite complex general KBM model of Eq. (1) for large temperature gradients, enabling further analytical analysis of this regime. For instance, the critical value for β for destabilisation based on Eq. (8) is derived in Appendix D in the local limit.

3.2.2. MODERATE TEMPERATURE GRADIENTS

For moderate temperature gradients the importance of the drift terms becomes evident. These terms are associated with the effects of the curvature and ∇B drifts, and generally cause a stabilisation of the mode.

Figures 3 and 4 summarize the results of the numerical computations of γ and ω_r with GENE and their corresponding values obtained from the variational approach for the case of moderate gradients ($R/L_{Ti,e} = 15$). The diamagnetic modification of ideal MHD $\big[$Eq. (8)$\big]$ (left plot in Fig. 3) does not longer adequately describe the mode. The second-order terms

of the long-wavelength limit [Eq.(10)] improve the agreement at small k_y (filled dots on the right plot of Fig. 3), while also providing an improving correction to ω_r, which is now above $\omega_{pi}/2$.

To extend the agreement to the finite-$k_y\rho_s$ region all second order of Eq. (9) terms can be retained. These terms tend to further stabilise the mode. The values of γ and ω_r resulting from the variational analysis of Eq. (9) [as well as its long wavelength limit Eq. (10)] are shown in Figs. 3 (right) and 4 for $R/L_{Ti,e} = 15$ and $R/L_{Ti,e} = 12.5, 20$ respectively. We observe very good agreement for growth rates, while frequencies are not as satisfactory. However, in the low-k_y end of the spectrum, where the mode is most unstable, the agreement between theory and code is still remarkable.

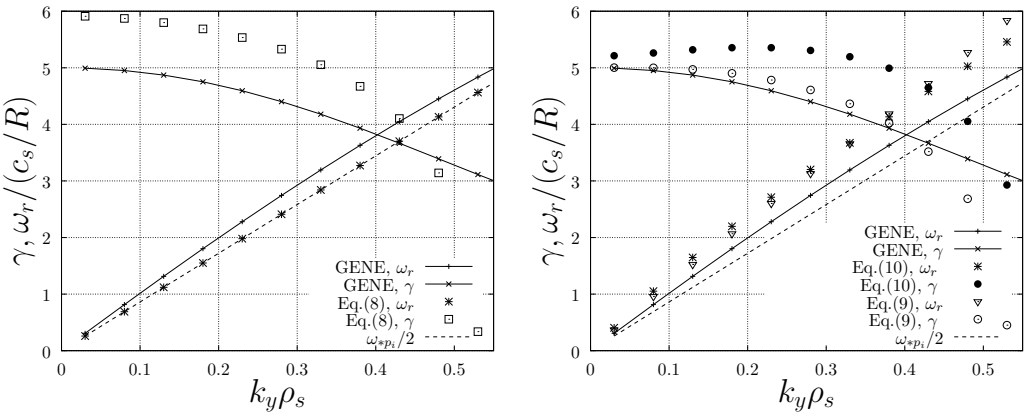

Figure 3. Spectra for $R/L_{Ti,e} = 15$. On the left GENE simulations γ: solid curve ($\times$) and ω_r: solid curve ($+$) against results obtained solving Eq. (8) (γ: squares and ω_r: stars) are presented. On the right results obtained solving Eq. (10) (γ: filled dots and ω_r: stars) and Eq. (9) (γ: open dots and ω_r: triangles) are presented. The dashed line represents the $\omega_{*pi}/2$ frequency.

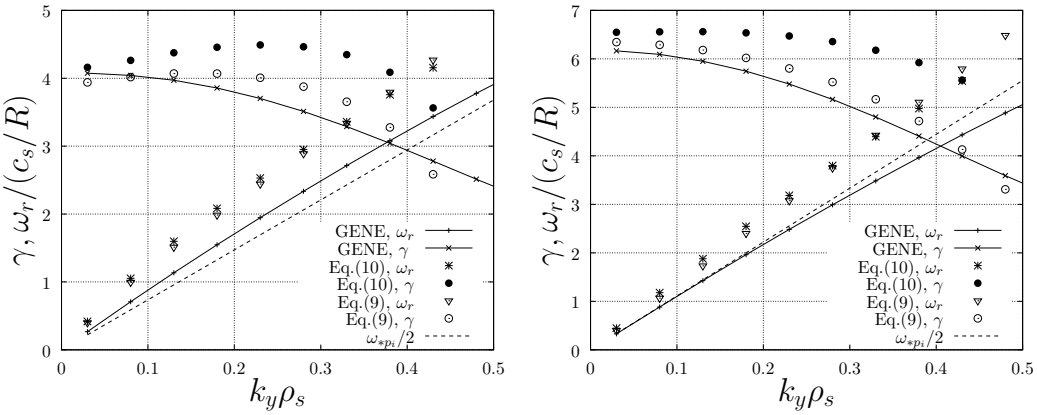

Figure 4. Spectra for $R/L_{Ti,e} = 12.5, 20$ from left to right respectively. GENE simulations γ: solid curve ($\times$) and ω_r: solid curve ($+$) against results obtained solving Eq. (10) (γ: filled dots and ω_r: stars) and Eq. (9) (γ: open dots and ω_r: triangles) are presented. The dashed line represents the $\omega_{*pi}/2$ frequency.

For even smaller temperature gradients ($R/L_{Ti,e} = 7.5$), the mode frequency falls in the interval $\omega_{pi} > \omega_r > \omega_{pi}/2$ for $k_y\rho_s > 0.3$ and $\omega_r > \omega_{pi}$ for $k_y\rho_s < 0.3$. The most unstable mode wavelength is $k_y\rho_i \approx 0.25$ (see Fig.5). Both these tendencies are captured correctly in Eqs. (9) and (10), while some other stabilising effect (e.g. Ion Landau Damping and finite-Larmor-radius effects) might be missing in the simplified model as the maximum growth rate exceeds the GENE prediction.

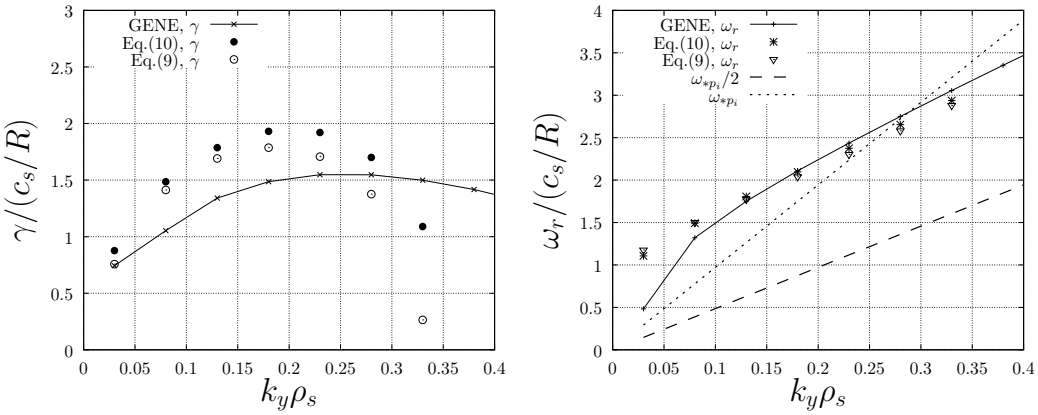

Figure 5. Spectra for $R/L_{Ti,e} = 7.5$. On the left GENE simulations γ: solid curve ($\times$) against results obtained solving Eq. (10) (γ – filled dots) and Eq. (9) (γ – open dots) are presented. On the right GENE simulations ω_r: solid curve (+) against results obtained solving solving Eq. (10) (ω_r: stars) and Eq. (9) (ω_r: triangles) are presented. The dashed line represents the $\omega_{*pi}/2$ frequency, and the dotted line represents the ω_{*pi} frequency.

IV. CONCLUSION

In the present work, we have revisited the problem of kinetic ballooning mode instability. We have derived an appropriate ordering for β, which allows us to greatly simplify previous KBM theories.

We introduced a variational approach to verify numerically the analytical results against linear GENE simulations, which are also repeated with GS2 code, demonstrating excellent agreement.

The results of the kinetic instability analysis and its comparison with numerics lead us to distinguish between "high temperature-gradient" and "moderate temperature-gradient" KBM regimes. The real frequency plays an important role in the identification of different KBM regimes.

For large temperature gradients instability occurs only for $\omega_r = \omega_{pi}/2$. The maximum growth rate occurs at very long wave length. In this case, if magnetic drifts are kept consistent with the equilibrium pressure gradient, the gyrokinetic codes show excellent quantita-

tive agreement with a diamagnetic modification of ideal MHD [Eq. (8)] derived in high-β ordering, generalizing the electromagnetic ITG theory of Ref. [7], which was specifically constructed for $\beta \sim \varepsilon^2$ and coincides with the present model for $\eta_i \gg 1$.

For moderate temperature gradients, we observe that the mode frequency tends to a value $\omega_{pi} > \omega_r > \omega_{pi}/2$ or even $\omega_r > \omega_{pi}$. The growth rate now peaks at finite k_y. This regime is described by Eq.(9), where all corrections connected with both high-$\beta \sim \varepsilon$ and $b \sim \varepsilon$ (which is especially important for finite $k_y\rho_i$) are included. The solution of Eq.(9) provides good agreement for growth rates and shows the correct trend for the mode frequency.

In our study, we did observe a destabilisation of KBMs when frequencies fall in the range $\omega_{pi} > \omega_r > \omega_{pi}/2$, but only for large to moderate pressure gradients. However, as R/L_p decreases towards marginal values, these conditions seem to be stabilizing (see Fig.5, where the code results show a decreasing growth rate for k_y such that $\omega_{pi} > \omega_r > \omega_{pi}/2$). Nevertheless, if we consider the discrepancy between the points in Fig.5, which come from the fluid approximation of Eqs. (9-10), and the solid line, generated by the full kinetic numerical simulation, Eqs. (9-10) seem to overestimate the growth rate for $\omega_r > \omega_{pi}$. For $\omega_{pi} > \omega_r > \omega_{pi}/2$, Eqs. (9-10) underestimate growth rates. This discrepancy for $\omega_{pi} > \omega_r > \omega_{pi}/2$ could perhaps be attributed to either resonant ion-transit destabilisation [15], or finite-Larmor-radius effects.

ACKNOWLEDGEMENTS

The authors are grateful to Dr. P. Helander and Dr. J. W. Connor for constructive comments and fruitful discussions, to Dr. M. Barnes for clarifying the role of the equilibrium pressure gradient in the $\hat{s}-\alpha$ model, to Dr. T. Görler, Dr. H. Doerk and Dr. P. Xanthopoulos for several discussions on the GENE code.

APPENDIX A (VELOCITY-SPACE INTEGRALS)

In the velocity-space integrals of Eqs.(3)-(5), we expand the denominator for $\omega_d \ll \omega$ and the Bessel functions for $b \ll 1$ to obtain:

$$Q \approx 2\int_0^\infty d\hat{v}_\perp \hat{v}_\perp \int_{-\infty}^\infty d\hat{v}_\parallel \frac{e^{-(\hat{v}_\parallel^2+\hat{v}_\perp^2)}}{\sqrt{\pi}}\Big\{1-\frac{\omega_{*i}}{\omega}\big[1+\eta_i\big(\hat{v}_\parallel^2+\hat{v}_\perp^2-\frac{3}{2}\big)\big]\Big\}\Big(1+\frac{\omega_B}{\omega}\hat{v}_\perp^2 + 2\frac{\omega_\kappa}{\omega}\hat{v}_\parallel^2\Big)\Big(1-\frac{k_\perp^2\rho_i^2}{2}\hat{v}_\perp^2\Big) \approx 1-\frac{\omega_{*i}}{\omega}+\left(\frac{\omega_B+\omega_\kappa}{\omega}-\frac{k_\perp^2\rho_i^2}{2}\right)\Big[1-\frac{\omega_{*i}}{\omega}(1+\eta_i)\Big] + \left(\frac{3\omega_\kappa^2+2\omega_B\omega_\kappa+2\omega_B^2}{\omega^2}-\left(\frac{\omega_B+\omega_\kappa}{\omega}\right)\frac{k_\perp^2\rho_i^2}{2}+\frac{\left(\frac{k_\perp^2\rho_i^2}{2}\right)^2}{8}\right)\Big[1-\frac{\omega_{*i}}{\omega}(1+\eta_i)\Big], \tag{15}$$

$$Q' \approx 2\int_0^\infty d\hat{v}_\perp \hat{v}_\perp \int_{-\infty}^\infty d\hat{v}_\parallel \frac{e^{-(\hat{v}_\parallel^2+\hat{v}_\perp^2)}}{\sqrt{\pi}}\Big\{1-\frac{\omega_{*i}}{\omega}\big[1+\eta_i\big(\hat{v}_\parallel^2+\hat{v}_\perp^2-\frac{3}{2}\big)\big]\Big\}\Big(1+\frac{\omega_d}{\omega}\Big)\frac{-2\hat{v}_\perp^2}{k_\perp\rho_i}\Big(\frac{k_\perp\rho_i}{2}\hat{v}_\perp^2 - \frac{3}{16}k_\perp^3\rho_i^3\hat{v}_\perp^3\Big) \approx -\Big[1-\frac{\omega_{*i}}{\omega}(1+\eta_i)\Big]-\frac{2\omega_B+\omega_\kappa}{\omega}\Big[1-\frac{\omega_{*i}}{\omega}(1+2\eta_i)\Big] + \frac{3}{4}k_\perp^2\rho_i^2\Big[1-\frac{\omega_{*i}}{\omega}(1+2\eta_i)\Big], \tag{16}$$

$$R \approx 2\int_0^\infty d\hat{v}_\perp \hat{v}_\perp \int_{-\infty}^\infty d\hat{v}_\parallel \frac{e^{-(\hat{v}_\parallel^2+\hat{v}_\perp^2)}}{\sqrt{\pi}}\Big\{1-\frac{\omega_{*i}}{\omega}\big[1+\eta_i\big(\hat{v}_\parallel^2+\hat{v}_\perp^2-\frac{3}{2}\big)\big]\Big\}\Big(1+\frac{\omega_d}{\omega}\Big)\hat{v}_\perp^4\Big(\frac{1}{4}\hat{v}_\perp^2 - \frac{\hat{v}_\perp^4}{16}k_\perp^2\rho_i^2\Big) \approx \frac{3}{2}\Big[1-\frac{\omega_{*i}}{\omega}(1+3\eta_i)\Big]+\frac{3}{2}\frac{(4\omega_B+\omega_\kappa)}{\omega}\Big[1-\frac{\omega_{*i}}{\omega}(1+4\eta_i)\Big] - \frac{3}{2}k_\perp^2\rho_i^2\Big[1-\frac{\omega_{*i}}{\omega}(1+4\eta_i)\Big]. \tag{17}$$

By substituting these results in Eq.(1), for $\beta \sim \varepsilon$, we obtained Eq.(8) of the text.

APPENDIX B (BENCHMARK, GENE-GS2 COMPARISON)

The computational results presented in this work were obtained with the GS2 and GENE codes. Both codes are used to solve the gyrokinetic equations in the local flux tube limit in five-dimensional phase space. In general, we observed a good agreement between the two codes.

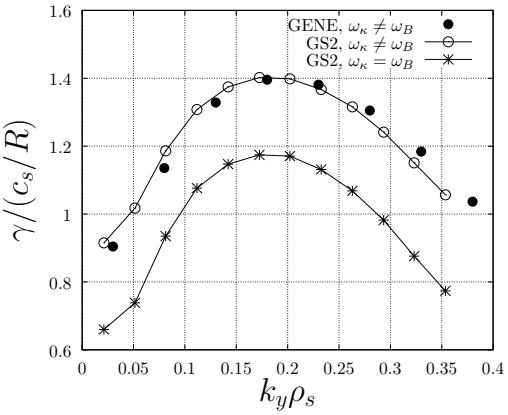

Figure 6. KBM spectra for $R/L_T = 6.89$, β=1.5% 1) GENE, $\omega_\kappa \neq \omega_B$, filled circles; 2) GS2, $\omega_\kappa \neq \omega_B$, open circles; 3) GS2, $\omega_\kappa = \omega_B$, stars.

The GS2 code was modified to take into account of the difference between curvature and ∇B drifts for finite equilibrium pressure gradients [Eqs. (13), (14) of the main text]. In Fig.(6) the growth rate for the KBM mode is shown for two cases: $\omega_\kappa \neq \omega_B$ [calculated with GENE (filled circles) and GS2 (open circles), good agreement is observed after the GS2 modification] and $\omega_\kappa = \omega_B$ (calculated with GS2, stars). Note the significant decrease of the growth rate in the latter case.

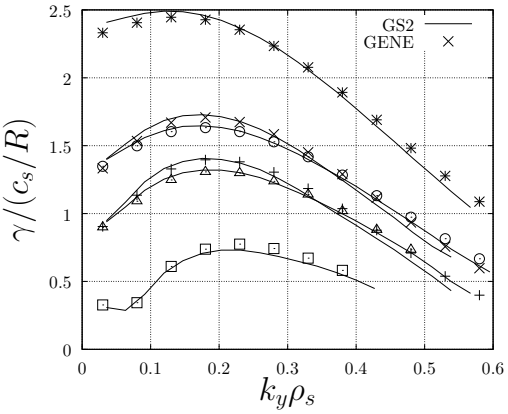

Figure 7. KBM spectra for several cases with different $L_{Ti,e}$.

Fig.(7) shows a good agreement between GS2 and GENE calculations for various q and

$R/L_{Ti,e}$ in a scenario based on Cyclone Base Case: $q = 1.4$, $R/L_{T_{i,e}} = 6.89$ (+), 7.5 (×), 9 (stars) and $q = 1.6$, $R/L_{T_{i,e}} = 4.5$ (squares), 5.5 (triangles), 6.1 (circles). We also note that calculation results presented in Fig.(1) are in a good agreement with other CBC studies [6], [14].

APPENDIX C (MAGNETIC SHEAR)

The GS2 calculation of the KBM linear growth rate as a function of the temperature gradient in the collisionless limit in shown in Fig. 8. The calculations are based on the Cyclone Base Case parameters in $\hat{s} - \alpha$ geometry. A flat density gradient and equal temperature for ions and electrons are assumed. Three values of the magnetic shear $\hat{s}$ are considered: 0.786, 0.486, 0.386.

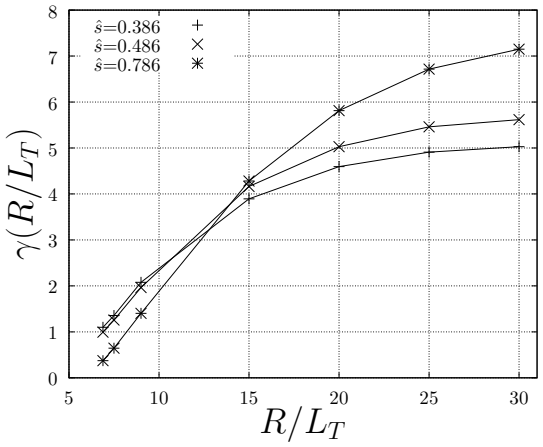

Figure 8. The linear growth rate of electromagnetic KBM mode, $\beta = 1.5\%$, with different magnetic shear $\hat{s}$.

In the low R/L_T domain lower magnetic shear leads to a higher KBM growth rate. The opposite is observed in the high R/L_T domain. The critical value of R/L_T is located between $R/L_T = 10$ and $R/L_T = 15$, which corresponds to the different KBM regimes discussed in Section III (i.e. the moderate and the high temperature gradient regimes).

APPENDIX D (LOCAL ANALYSIS)

If we consider the simple case in which the equilibrium magnetic field is independent of the coordinate along $\mathbf{B}$ and $k_\perp^2 = k_y^2$ then, after Fourier transformation, Eq. (8) becomes

$$\frac{b}{\beta_i}\frac{k_z^2 v_{thi}^2}{\omega^2} = \frac{\omega_B + \omega_\kappa}{\omega^2}\omega_p + \frac{k_y^2\rho_i^2}{2}\left[1 - \frac{\omega_{*i}}{\omega}\left(1+\eta_i\right)\right] + \frac{\beta_i}{2}\frac{{\omega_p}^2}{\omega^2}.$$

Let us set $\omega = \omega_r + i\gamma$, then

$$\omega_r^2 - \omega_r\omega_{*i}\left(1+\eta_i\right) - \gamma^2 = \frac{1}{\beta_i}k_z^2 v_{thi}^2 - \frac{\beta_i}{2b}\omega_p^2 - \frac{\left(\omega_B+\omega_\kappa\right)\omega_p}{b},$$

which allows us to find:

$$\omega_r = \frac{1}{2}\omega_{*i}\left(1+\eta_i\right) = \frac{k_y\rho_i}{4}\frac{v_{thi}}{R}\frac{R}{L_n}\left(1+\eta_i\right), \tag{18}$$

$$\gamma = \sqrt{-\left[\frac{k_y\rho_i}{4}\frac{v_{thi}}{R}\frac{R}{L_n}\left(1+\eta_i\right)\right]^2 - \left[\frac{1}{\beta_i}k_z^2 v_{thi}^2 - \frac{\beta_i}{2b}\omega_p^2 - \frac{\left(\omega_B+\omega_\kappa\right)\omega_p}{b}\right]}. \tag{19}$$

The stability condition is:

$$\left[\frac{k_y\rho_i}{4}\frac{v_{thi}}{R}\frac{R}{L_n}\left(1+\eta_i\right)\right]^2 < \left[-\frac{1}{\beta_i}k_z^2 v_{thi}^2 + \frac{\beta_i}{2b}{\omega_p}^2 + \frac{\left(\omega_B+\omega_\kappa\right)\omega_p}{b}\right].$$

To evaluate k_{ymax} of the maximum growth rate we set $\partial_{k_y}[\gamma\left(k_y\right)] = 0$, thus obtaining:

$$k_{ymax} = 0.$$

This is consistent with the nonlocal analysis at large pressure gradients. From Eq.(18)-(19) and considering $k_{ymax} = 0$:

$$\omega_r(k_{ymax}) = 0,$$

$$\gamma(k_{ymax}) = \sqrt{-\frac{1}{\beta_i}k_z^2 v_{thi}^2 + \frac{\beta_i}{2b}\omega_p^2 + \frac{\left(\omega_B+\omega_\kappa\right)\omega_p}{b}}.$$

From Eq.(19), we see that instability occurs for:

$$4\left[-\frac{1}{\beta_i}k_z^2 v_{thi}^2 + \frac{\beta_i}{2b}\omega_p^2 + \frac{\left(\omega_B+\omega_\kappa\right)\omega_p}{b}\right] > \omega_{*i}^2\left(1+\eta_i\right)^2,$$

which allows us to derive the expression for a critical β in this local limit:

$$\beta_i > \frac{b}{8}\left(1-\eta_i\right)^2\frac{\omega_{*i}^2}{\omega_p^2} - \frac{\omega_B}{\omega_p} + \sqrt{\left[\frac{\omega_B}{\omega_p} - \frac{b}{8}\left(1-\eta_i\right)^2\frac{\omega_{*i}^2}{\omega_p^2}\right]^2 + b\frac{k_z^2 v_{thi}^2}{\omega_p^2}} \equiv \beta_{diam},$$

or, at very long wave length:

$$\beta_{diam} = \sqrt{\frac{\omega_B}{\omega_p}\left[\frac{\omega_B}{\omega_p} + 2\beta_2\right]} - \frac{\omega_B}{\omega_p},$$

where $\beta_2 = bk_z^2 v_{thi}^2/(2\omega_B\omega_p)$, which would be β_{MHD} of Ref.[7] for $\beta_i \sim \varepsilon^2$. By expressing explicitly all quantities in terms of R/L_p, k_z and q we find:

$$\beta_{diam} \sim \frac{L_p}{R}\left\{\sqrt{1+2k_z^2R^2} - 1\right\} = \frac{L_p}{R}\left\{\sqrt{1+\frac{2}{q^2}} - 1\right\},$$

which gives us for small q value:

$$\beta_{diam} \sim \frac{1}{q}\frac{L_p}{R},$$

and for large q:

$$\beta_{diam} \sim \frac{1}{q^2}\frac{L_p}{R}.$$

These limits are reported for the sake of completeness and should be taken *cum grano salis*.

---

[1] J.W. Connor, R.J. Hastie, and J.B. Taylor, Phys. Rev. Lett. 40 (1978)

[2] M. Thomas, Jr. Antonsen and Barton Lane Phys. Fluids 23, 1205 (1980)

[3] W. M. Tang, J. W. Connor, and R. J. Hastie, Nucl. Fusion 20, 1439 (1980)

[4] R.E. Waltz and R.L. Miller, Phys. Plasmas 6, 4265 (1999)

[5] M. Kotschenreuther, W. Dorland, Q. Liu, M. Zarnstorff, R. Miller and Y. Lin-Liu, Nucl. Fusion 40, 677 (2000)

[6] E. A. Belli and J. Candy, Phys. Plasmas 17, 112314 (2010)

[7] A. Zocco, P. Helander and J. W. Connor, Plasma Phys. Control. Fusion 57(8) (2015)

[8] M. Kotschenreuther, G. Rewoldt, and W.M. Tang, Comput. Phys. Commun. 88, 128 (1995)

[9] W. Dorland, F. Jenko, M. Kotschenreuther, and B.N. Rogers, Phys. Rev. Lett. 85, 5579 (2000)

[10] F. Jenko, W. Dorland, M. Kotschenreuther, and B.N. Rogers, Phys. Plasmas 7, 1904 (2000)

[11] T. Dannert and F. Jenko, Phys. Plasmas 12, 72309 (2005)

[12] K.V. Roberts and J.B. Taylor, Phys. Rev. Lett. 8, 197 (1962)

[13] A.M. Dimits, G. Bateman, M.A. Beer, B.I. Cohen, W. Dorland, G.W. Hammett, C. Kim, J.E. Kinsey, M. Kotschenreuther, A.H. Kritz, L.L. Lao, J. Mandrekas, W.M. Nevins, S.E. Parker, A.J. Redd, D.E. Shumaker, R. Sydora, and J. Weiland, Phys. Plasmas 7, 969 (2000)

[14] A. Ishizawa, S. Maeyama, T.-H. Watanabe, H. Sugama and N. Nakajima, J. Plasma Phys. 81, 435810203 (2015)

[15] S.T. Tsai, L. Chen, Phys. Fluids B 5, 3284 (1993)